J Mater Sci: Mater Electron **(2026) 37:519**

Effect of temperature on the stability of nickel sulfide reduced graphene oxide nanocomposite counter electrode in quantum dot-sensitized solar cells

Layla Haythoor Kharboot[1,2], Abdillah Sani Mohd Najib[1,3], Tuty Asma Abu Bakar[1,3], Norhuda Hidayah Nordin[4], Andi Erwin Eka Putra[5], Ataf Ali Altaf[6], and Nor Akmal Fadil[1,3,*]

[1] *Department of Materials, Manufacturing, and Industrial Engineering, Faculty of Mechanical Engineering, Universiti Teknologi Malaysia, Skudai, 81310 Johor Bahru, Johor, Malaysia*
[2] *Department of Renewable Energy Engineering, University of Al-Hussain College, Karbala, Iraq*
[3] *Materials Research and Consultancy Group, Faculty of Mechanical Engineering, Universiti Teknologi Malaysia, Skudai, 81310 Johor Bahru, Johor, Malaysia*
[4] *Department of Manufacturing and Material Engineering, International Islamic University Malaysia, Jalan Gombak, 53100 Kuala Lumpur, Selangor, Malaysia*
[5] *Waste to Energy Research Group, Hasanuddin University, 90245 Makassar, Indonesia*
[6] *Department of Chemistry, University of Okara, Okara 56300, Pakistan*

Received: 13 September 2025
Accepted: 19 February 2026
Published online: 8 March 2026

ABSTRACT

Quantum dot-sensitized solar cells (QDSSCs) are equipped with counter electrodes (CEs) based on reduced graphene oxide (rGO) and nickel sulfide (NiS/rGO). A hydrothermal method performed at 150 °C with variable reaction times (5, 10, and 15 h) was used to synthesize NiS/rGO CEs and evaluate their electrocatalytic activity and stability by exposing them to varying conditions at 25, 40, 60, and 80 °C for 100 h. Electrochemical performance was assessed through cyclic voltammetry (CV), electrochemical impedance spectroscopy (EIS), and Tafel polarization. Results showed that NiS/rGO 5 h exhibited superior electrocatalytic activity, achieving a significantly higher current density. CV results showed that NiS/rGO 5 h generated the highest current density of 112.4 mA/cm^2 at 80 °C (Pt = 8.1 mA/cm^2), and lower charge-transfer resistance (R_{ct} values, 3.6 Ω cm^2 at 80 °C than (Pt = 674.4 Ω cm^2). The high performance was attributed to the dominance of β-NiS phase. Additionally, the nanocomposites demonstrated strong mechanical adhesion and stability under prolonged exposure to elevated temperatures. This study highlights the potential of NiS/rGO nanocomposites as cost-effective and efficient alternatives to Pt for improved QDSSC performance.

Address correspondence to E-mail: norakmal@utm.my

https://doi.org/10.1007/s10854-026-16855-3

1 Introduction

Photovoltaic systems utilizing solar irradiation face challenges in efficiency due to increased internal carrier recombination rates and thermal effects. These affect the catalytic activity of electrode materials of CE, affecting overall performance and efficiency. Photovoltaic systems rely on electrocatalytic materials like platinum (Pt) for efficiency and durability. However, platinum's non-catalytic nature can lead to overpotential in electrolyte regeneration, reducing power conversion efficiency. This is due to the absorption of S^{2-} on the surface, diminishing Pt's surface activity and causing poisoning of the CE. Therefore, selecting the right materials is crucial for optimizing CE systems [1–3].

CE materials are being researched to overcome Pt's drawbacks by substituting Pt with transition metal sulfide (TMS) which has unique physical and chemical characteristics. TMS CEs offer cost-effectiveness, exceptional electrochemical activity, and robust mechanical and thermal stability, making them a promising alternative for QDSSC. TMS CEs such as PbS [4], NiS [5], CoS [6], FeS [7], and Cu_xS [8] have led to remarkable improvements in photovoltaic operations.

However, Hodes et al. [9] and Zeng et al. [10] identified mechanical instability and uncertainties in Cu_2S and CoS-based CEs, attributed to the chemical reaction between copper and the electrolyte, which leads to surface poisoning of the photoelectrode. Additionally, Gopi et al. [4] showed that PbS CEs in QDSSCs face more challenges than other metal sulfides due to their electrochemical properties, such as electron transfer rate and interaction with the electrolyte, which could lead to less efficient electron transfer, reduced catalytic activity, and stability issues under operational conditions.

Device performance in solar PV cells is significantly influenced by the stability of catalyst materials used in counter electrodes (CEs) in QDSSCs, particularly for non-precious metals and alloys. It is crucial to study temperature stability and strengthen CE stability through strong electrode adhesion, as solar PV cells' exposure to outdoor temperatures affects the efficiency of energy conversion. Extensive research on dye-sensitized solar cells (DSSCs) was conducted by O'Regan and Grätzel [11]. These cells have gained significant attention due to their low cost and relatively high energy conversion efficiency [12–14]. In recent years, numerous researchers have revealed that narrow band-gap semiconductor quantum dots (QDs), such as CdS (QDs) [15], CdS/CdSe (QDSs) [16], $CuInS_2$ (QDs) [17], PbS (QDs) [18], and CdS/CdSe/ZnS (QDs) [4, 6, 8], are being introduced as photosensitizers for solar cells. These are called Quantum dot-sensitized solar cells (QDSSCs). The semiconductor quantum dots are used as photosensitizers, converting absorbed photons to excitons. They have several advantages including size-tunable band gaps, excellent photostability, high absorption coefficient, long carrier lifetime, and high dipole moment defining the extent to which a specific wavelength's material light can penetrate before it is absorbed, large intrinsic dipole moment, and the ability to generate multiple excitons from a single photon called multiple exciton 'generation' (MEG) [4, 19–22].

Due to these remarkable properties, QDSSCs can potentially achieve theoretical efficiencies surpassing 44%, exceeding the Shockley–Queisser detailed limit of 33% for thin-film solar cells as reported by Pawar et al. [23]. This remarkable promise places them significantly ahead of their counterparts such as dye-sensitized solar cells (DSSCs) which have an efficiency of 31% as indicated by Yeh et al. [24]. Consequently, researchers are increasingly turning their attention toward QDSSCs, recognizing them as a transformative force in the realm of solar energy conversion.

Nickel sulfides, classified as TMS materials, exhibit unique optical, electrochemical, and magnetic properties, are eco-friendly, and can be synthesized into sulfur-rich compounds like Ni_3S_4 and NiS_2 [25–27]. Nanostructured nickel sulfide CEs exhibit low charge transfer resistance, high short-circuit current, enhanced electrocatalytic activity, CE stability, improved PV performance, and exceptional stability in polysulfide electrolytes [4, 28]. To improve catalyst performance and stability, the catalyst material must be uniformly distributed and securely attached to the CE, ensuring chemical inertness against the corrosive electrolyte [29].

Reduced graphene oxide (rGO) is a crucial material for improving catalytic activity and efficiency as a support material. It increases active sites, maintains catalyst stability, and enhances selectivity. It promotes even particle dispersion, boosting reaction rate. Moreover, rGO enhances the catalysts' physical properties, like electrical conductivity, and reduces the need for expensive materials [30–32]. NiS/rGO nanocomposites CE are ideal for high-performance electrochemical devices, similar to the CuS/rGO combination which

integrates catalytic nickel sulfide nanoparticles with electrically conductive rGO [14, 33–35]. Previous studies on NiO–Co_3O_4–rGO (for nitrite detection) and MoS_2/Ni_3S_2–rGO (for alcohol fuel cells) demonstrated that rGO enhances conductivity, prevents particle agglomeration, increases catalytic sites, and improves long-term stability. This confirms that, even in NiS/rGO work for QDSSCs, rGO plays a universal role in boosting conductivity, electrocatalytic activity, and stability of transition metal nanocomposites [36, 37].

The performance of materials depends on their valence state and morphology, which facilitate easy access to electrolytes, leading to high electrochemical performance [25]. The stability of QDSSCs is influenced by various factors, including QD type, photoanode, CE electrocatalytic behavior, and electrolyte. Specific processes affecting performance stability are challenging to estimate due to the diverse degradation mechanisms [38].

Gopi and his colleagues [4] demonstrated the excellent electrochemical performance of nickel sulfide-based CEs across various surface morphologies, but did not explore their electrochemical and mechanical stability at different temperatures [5, 39] and furthermore did not incorporate rGO. Incorporating rGO can significantly enhance conductivity and the surface area, thereby improving the performance of CEs. The absence of rGO means missing out on these benefits, underscoring its importance in achieving optimal electrocatalytic efficiency and stability in such systems.

In short, the search for material substitutes for precious metals for the CE of QDSSCs at high temperatures, utilizing TMS and incorporating rGO, is still incomplete. Therefore, it is essential to conduct a study that focuses exclusively on the stability of CE at various temperatures, ignoring other QDSSC components. By utilizing nickel sulfide nanocomposites, electrocatalytic activity and stability can be enhanced further through the synergistic effects of highly catalytic nickel sulfide nanocomposites and electrically conductive rGO. Electrochemical testing should be conducted, as well as characterization of materials before and after the exposure test, to determine CE's stability over 100 h at various temperatures and to document the extent to which CE stability is maintained as a function of temperature.

The hydrothermal synthesis method enables precise control over the growth of NiS/rGO nanostructures, yielding a material with a substantial surface area that translates into improved electrocatalytic performance. These results showcase a noteworthy increase in power conversion efficiency when compared to conventional counter electrode (CE) materials. Furthermore, QDSSCs employing the NiS CE catalyst demonstrate outstanding operational stability over extended periods, underscoring its potential for practical application in real-world scenarios.

This study proposes an innovative approach to developing efficient and durable counter electrode (CE) catalysts for QDSSCs, contributing to the advancement of next-generation solar energy technologies. The research focuses on the synthesis and characterization of a NiS/rGO nanocomposite CE, highlighting its enhanced catalytic activity in facilitating the redox couple reduction within QDSSCs. Building on the synthesis method established by Gopi et al. [4], with the addition of reduced graphene oxide (rGO) as a supporting material, this study also introduces improvements in temperature variation and electrochemical stability testing. The amount of rGO added to nickel sulfide was selected based on preliminary experimental trials and supported by literature reports [14, 31, 32]. The chosen ratio provided the best compromise between catalytic activity, electrical conductivity, and device stability, thereby justifying its use in this work.

The objective is to investigate the effects of different temperature conditions on the electrochemical stability of the NiS/rGO CE for 100 h, and to compare its performance with that of NiS nanoparticles (NiS Nps) and platinum (Pt) CEs. The selected temperatures (25, 40, 60, and 80 °C) were based on light soaking tests used in previous studies on the performance of DSSCs [29, 40–44].

2 Experimental details

2.1 Materials

Nickel(II) nitrate hexahydrate ($Ni(NO_3)_2{\cdot}6H_2O \geq 99\%$) was used as the nickel precursor; thiourea ($CH_4N_2S \geq 99\%$) as sulfur precursor; ethanol (C_2H_5OH ~ 99.8%); polyethylene glycol (PEG MW ~300); sodium sulfide ($Na_2S\ 9H_2O \geq 98\%$), sulfur (S), graphene oxide (GO), potassium chloride (KCl, ≥ 99%), methanol (CH_3OH ~99.8%); distilled (DI) water; Nafion; isopropanol. All chemicals used in this research were purchased from Sigma-Aldrich, except for sodium sulfide which was purchased from Uni-Chem and used as

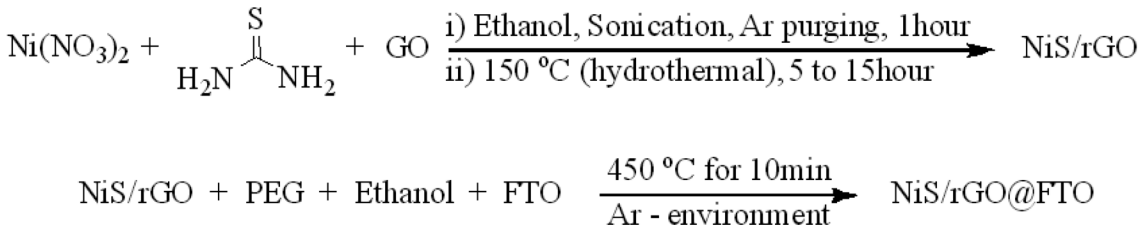

Scheme 1 Synthesis scheme of NiS/rGO nanocomposite without and with FTO substrate, where GO is the graphene oxide, rGO is the reduced graphene oxide, PEG is the polyethylene glycol, and FTO is the fluorinated tin oxide glass

received without further treatment. The substrate for CE is a fluorine-doped tin oxide (FTO, 13 Ω/sq^2, Hartford Glass Co. Inc.) with an active area of 10 × 10 mm. These materials remained in purified analytical form and were utilized as received.

2.2 Preparation of rGO and NiS/rGO nanocomposite

Since this study focuses on the catalytic performance and stability of the counter electrode (CE), the fabrication process primarily involved the synthesis of NiS/rGO and its deposit onto a fluorine-doped tin oxide (FTO) glass substrate. The synthesis procedure follows methods and parameters reported in the literature [4, 14]. All chemicals used to fabricate the NiS/rGO nanocomposites were utilized as received without further purification as shown in Scheme 1 and Fig S1.

The NiS/rGO nanocomposite synthesis began with the preparation of a Ni–S precursor solution. Specifically, 91 mg of nickel(II) nitrate hexahydrate ($Ni(NO_3)_2$ $6H_2O$) and 95 mg of thiourea (CH_4N_2S) were dissolved in 50 mL of ethanol to form a homogeneous solution. This mixture was transferred to a round-bottom flask, purged with argon gas to prevent oxidation, and stirred for 5 min using a magnetic stirrer. Then, 81 mg of graphene oxide (GO) was added, and the solution underwent ultrasonic treatment for 60 min to ensure uniform dispersion. The resulting solution was poured into a 100-mL Teflon-lined stainless-steel autoclave and subjected to hydrothermal treatment at 150 °C for 5, 10, and 15 h, followed by natural cooling to room temperature. The resulting precipitate was collected via centrifugation at 4000 rpm for 20 min, washed multiple times with distilled water and absolute ethanol until the pH was approximately 7, and dried under vacuum for 10–20 min. Finally, the sample was treated with argon gas to remove residual oxygen.

For deposition, the FTO glass substrate was ultrasonically cleaned with acetone, ethanol, and distilled water for 10 min each. The conductive side of the substrate was identified using a multimeter before preparing the NiS/rGO paste. This paste was formulated by thoroughly mixing 30 mg of NiS/rGO with polyethylene glycol and ethanol in a (1:1 ratio) using a mortar and pestle until a smooth consistency was achieved. Using the doctor blade method, the paste was then uniformly applied to the conductive side of the FTO glass (active area: 1 cm^2). After deposition, the coated substrate was heated in an oven at 450 °C for 10 min under an argon atmosphere to remove residual oxygen, ensuring a well-adhered and stable counter electrode suitable for catalytic applications.

2.3 Preparation of the electrochemical cell

In this study, two main procedures were used to measure the electrochemical stability and mechanical stability of the samples exposed to temperatures of 25, 40, 60, and 80 °C. Firstly, the electrochemical activity and electrochemical stability of NiS/rGO synthesized at various hydrothermal reaction times (5, 10, 15 h) and Pt CEs were measured using cyclic voltammetry (CV), electrochemical impedance spectroscopy (EIS), and Tafel polarization measurements. These analyses were conducted using the electrochemical cell (potentiostat instrument) containing three electrodes. The three electrodes are glassy carbon (GC) as a working electrode, Ag/AgCl as a reference electrode, and carbon as a CE, with polysulfide as an electrolyte.

The preparation of the electromechanical cell was contingent on the proper preparation of the working electrode, as detailed in Fig S2(1). The process involved combining 2 mg of the sample NiS/rGO nanocomposites (5, 10, 15 h) with a 200-µL solution containing 10-µL Nafion (5%, equivalent weight 1100, Aldrich), 50-µL isopropanol, and 140-µL ethanol. The

mixture was then ultrasonicated for 30 min. Subsequently, only 10μL of the mixture was dropped onto the GC's surface area and left to dry for a few minutes, as described by Zaman et al. [45].

The GC's surface area (0.2 cm^2), in the case of Pt (surface area 2 cm^2), was used as an exposed area of the working electrode (WE) directly. Once prepared, the working electrode was immersed along with the other two electrodes in a polysulfide electrolyte. Figure S2(2) illustrates the preparation of the polysulfide electrolyte combining 1 M $Na_2S{\cdot}9H_2O$, 2 M S, and 1 M KCl in methanol:DI water (7:3). The mixture was then stirred for 10 min using a magnetic stirrer plate. Methanol was mixed with DI water to reduce the high surface tension of the aqueous solution. Furthermore, this electrolyte was used to fill the space between the two electrodes (the active area is cm^2). The electrochemical cell was placed in a bath on a hot plate. The temperature was set to 25, 40, 60, and 80 °C, respectively, and monitored with a thermometer, as depicted in Fig S2(3). Ultimately, the electrochemical cell was connected to a potentiostat instrument (VersaSTAT 3F), and the device was set according to the performance test to be conducted.

2.4 Characterization techniques

The morphology and microstructure of the as-synthesized composites were observed using field emission scanning electron microscopy (FE-SEM, SU8020, Hitachi), equipped with on-system energy-dispersive X-ray spectroscopy (EDS) at an operating voltage of 15 kV. The phase purity was characterized, and structural analysis of the as-synthesized samples was performed using powder X-ray diffraction (XRD, Rigaku, model: SmartLab, 0.2 mSv/j), using Cu-K radiation with a wavelength of 0.154 nm and operated at 40 kV and 40 mA. X-ray photoemission spectroscopy (XPS) was performed using a VG Scientific ESCALAB 250 with monochromatic 177 Al–Kα radiation of 1486.6 eV and an electron take-off angle of 90°. High-resolution transmission electron microscopic (HR-TEM) analysis was achieved by the JEM-ARM200F TEM instrument. The JEM-ARM200F TEM instrument achieved a high-resolution transmission electron microscopic (HR-TEM) analysis. Cyclic voltammetry (scan rate of 100 mV/s), EIS, and Tafel polarization (with a scan rate of 10 mV/s) were performed using a BioLogic potentiostat/galvanostat/EIS analyzer (SP-150, France) for the three-electrode cells with NiS as working electrode, Ag/Ag Cl as reference electrode, and carbon as the counter electrode. Pt plate was used as the working electrode in a frequency range of 100–100 kHz.

3 Results and discussion

3.1 Characterization tests

X-ray photoelectron spectroscopy survey spectra with a photon energy of 1486.7 eV were performed to investigate the stoichiometry and chemical bonding properties of the NiS/rGO (5, 10, and 15 h) samples, as shown in Fig. 1a.

Figure 1 shows the X-ray photoelectron spectroscopy (XPS) survey and high-resolution spectra of the NiS/rGO samples synthesized at 5, 10, and 15 h using a photon energy of 1486.7 eV. Figure 1a confirms the presence of key elements. The C 1s spectra (Fig. 1b) for 5 h exhibit peaks at 284.4 ± 0.1 eV (C–C), 284.9 (C–O), 286.1 (C=O), and 289.1 eV (O–C=O), with similar peaks for 10 h (284.4, 284.8, 285.6, 288.9 eV) and 15 h (284.4, 284.9, 285.9, 289.0 eV). The dominant C–C peak and weaker oxygenated peaks confirm reduction of GO to rGO. Minor peaks near 285–287 eV suggest C–Ni bonding. In the Ni 2p spectra (Fig. 1c), 5 h shows peaks at 854.9 ($Ni^{3+}2p^{3/2}$), 855.6 ($Ni^{2+}2p^{3/2}$), 862.2, 874.5, and 883.4 eV. Similar peaks are seen for 10 h (854.7, 859.2, 862.3, 875.0, 882.3 eV) and 15 h (854.7, 858.8, 864.7, 875.2, 881.1 eV), indicating Ni^{2+} and Ni^{3+} states. O 1*s* spectra (Fig. 1d) show peaks at 532.4 (C=O), 533.7 (C–O) and 534.2 eV (O–C=O) for 5 h, with similar values for 10 h and 15 h, confirming rGO presence. S 2*p* spectra (Fig. 1e) for 5 h show peaks at 162.5 and 163.6 eV (S^{2-}), and at 164.5, 167.9, and 168.6 eV (C–S, O–S, O=S). Similar peaks were observed for 10 and 15 h, indicating evolving sulfur bonding over time.

The crystalline structures of NiS/rGO nanocomposites synthesized at different durations (5, 10, and 15 h) were analyzed via X-ray diffraction (XRD), as shown in Fig. 2. The hydrothermal method facilitated the in situ growth of NiS nanoparticles on reduced graphene oxide (rGO) surfaces, helping to achieve narrower particle size distributions and improved dispersion. The XRD pattern of GO showed a peak at 10.3°, associated with an interlayer spacing of 0.858 nm, while rGO showed a characteristic (002) reflection peak at 26.5°, consistent with previous reports [46].

Figure 2a presents the XRD patterns of NiS/rGO nanocomposites, where distinct peaks at 31.6°, 34.7°,

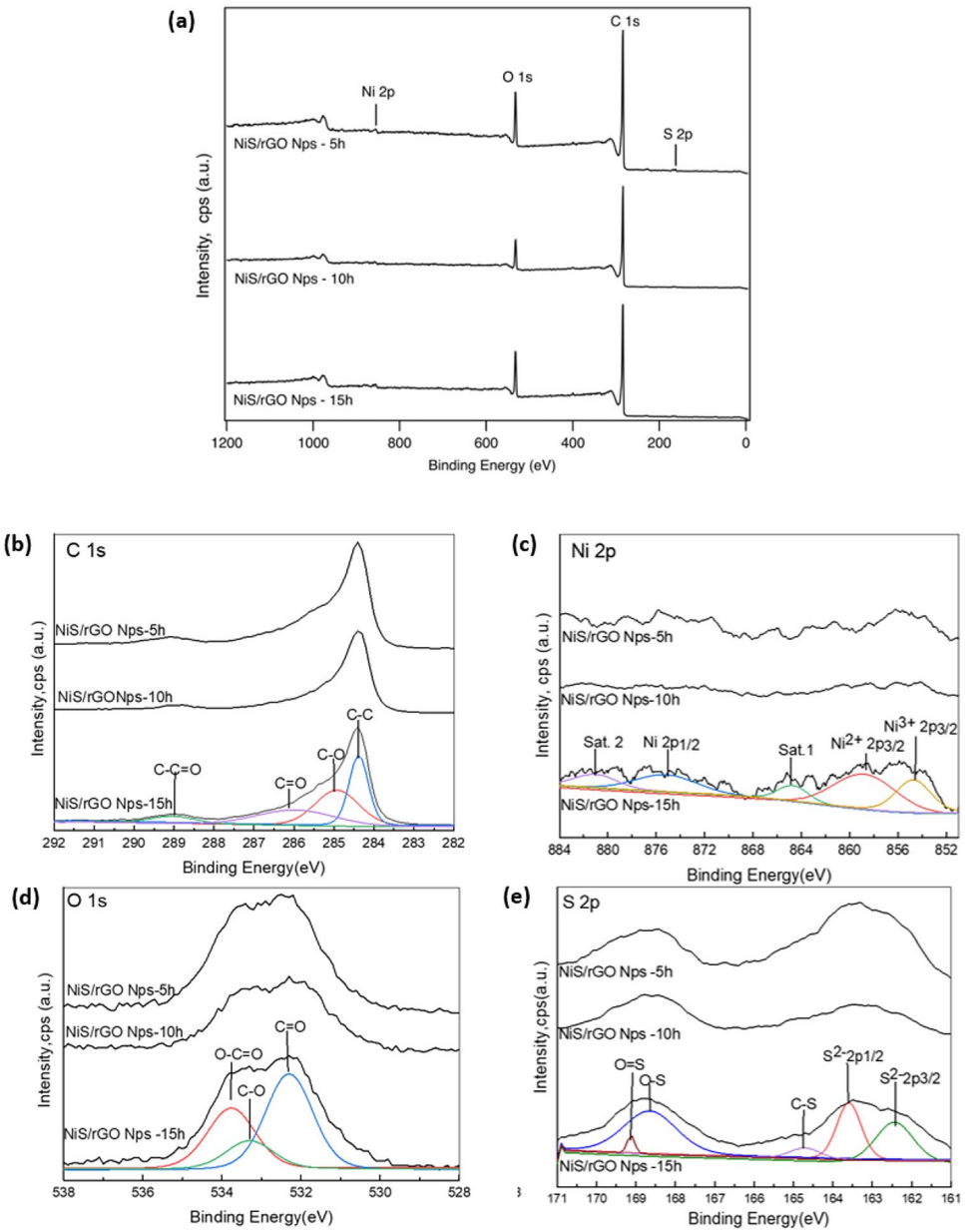

Fig. 1 XPS survey spectra **a** and high-resolution XPS spectra of NiS/rGO-(5 h, 10 h, and 15 h) at **b** C 1 *s*, **c** Ni 2*p*, **d** O 1 *s*, and **e** S 2*p* regions

46.0°, and 53.5° are indexed to the (100), (101), (102), and (110) planes of the α-NiS phase (JCPDS card no. 00-02-1280). Additional peaks at 18.4°, 30.3°, and 32.2° represent the (110), (101), and (300) planes of the rhombohedral β-NiS phase (JCPDS card no. 01-086-2281). Furthermore, diffraction peaks at 21.7°, 31.1°, 38.7°, 50.1°, and 78.1° confirm the presence of Ni_3S_2 (JCPDS card no. 00-44-1418), indicating the formation of a multiphase Ni–S structure. These findings align with previous studies [47, 48], ensuring reproducibility.

Figure 2b shows XRD of the samples deposited on FTO glass using the doctor blade technique and sintered at 450 °C. The patterns reaffirm the coexistence of α-NiS, β-NiS, and Ni_3S_2 phases. Peaks from the FTO substrate appear at 26.6°, 33.9°, 37.9°, 51.7°, 61.9°, 65.9°, and 78.7°, corresponding to the SnO_2 rutile structure (JCPDS card no. 00-41-1445). The rGO peak at 26.47° was consistently present. These comprehensive XRD results confirm the successful synthesis and structural integrity of NiS/rGO nanocomposites on FTO substrates.

To analyze the surface morphology of the NiS/rGO nanocomposites synthesized at varying durations (5, 10, and 15 h), field emission scanning electron

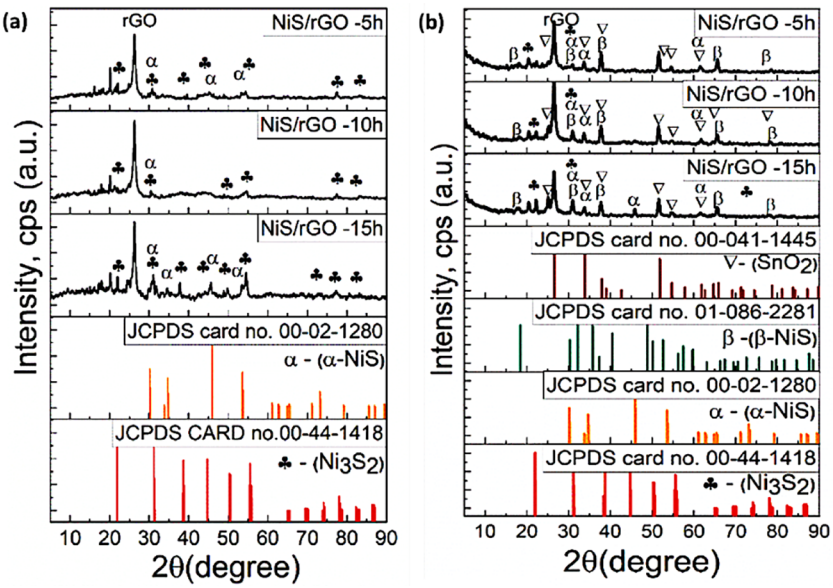

Fig. 2 XRD patterns for the as-synthesized nanocomposite samples NiS/rGO-(5 h, 10 h and 15 h) (**a**) and the deposited nanocomposite on the FTO substrate (**b**)

microscopy (FESEM) was employed, and the corresponding images are shown in Fig. 4. The NiS/rGO-5 h and NiS/rGO-10 h samples (Fig. 3a, b) exhibit uniformly dispersed spherical nanoparticles. However, NiS/rGO-15 h (Fig. 3c) displays nanoflower-like-spherical structures, indicating morphological evolution with increased synthesis time. As the reaction time increased, the surface morphology became rougher and more agglomerated, likely due to particle overgrowth. The average particle sizes measured using ImageJ software were approximately 0.5 μm for 5 h, 0.4 μm for 10 h, and 0.6 μm for the 15 h samples, with size distribution curves determined from 80 randomly selected nanoparticles. The nickel sulfide nanoparticles densely coated the rGO sheets, making the rGO structure barely visible.

To further confirm the elemental distribution and nickel sulfide phases, energy-dispersive X-ray spectroscopy (EDS) was conducted (Fig. 4). The elemental mapping showed high carbon content, verifying the presence of rGO. The Ni:S atomic ratios in NiS/rGO-5 h (3:2 and 3:2.4) indicated the predominance of the Ni_3S_2 phase. In contrast, the NiS/rGO-10 h and 15 h samples exhibited higher sulfur content, consistent with the formation of α-NiS. These findings align with the XRD results (Fig. 2), confirming that synthesis time plays a critical role in defining the nickel sulfide phase within the rGO matrix. Overall, both FESEM and EDS analyses demonstrate successful incorporation and structural tuning of nickel sulfide on the rGO nanosheets based on the synthesis duration.

To investigate the surface morphology and structural properties of the NiS/rGO nanocomposites deposited on the FTO glass substrates, FESEM, EDS, and HR-TEM analyses were conducted (Figs S1, S4). Figure S3 displays the FESEM images of the NiS/

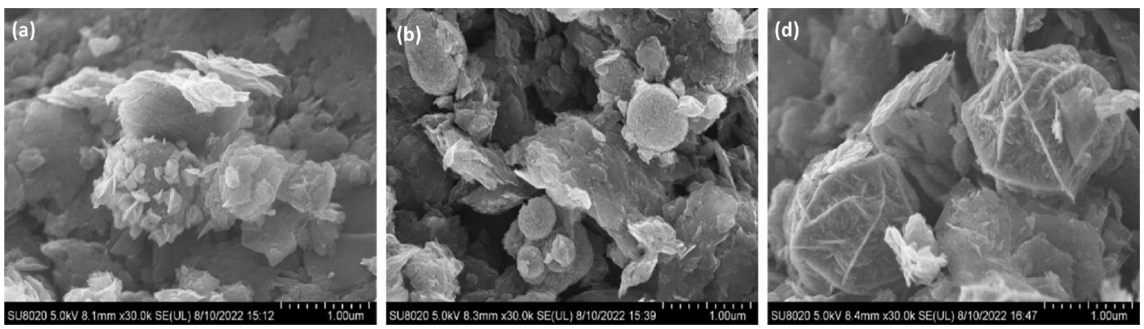

Fig. 3 FESEM images of NiS/rGO nanocomposite samples: **a** NiS/rGO-5 h, **b** NiS/rGO-10 h, and **c** NiS/rGO-15 h

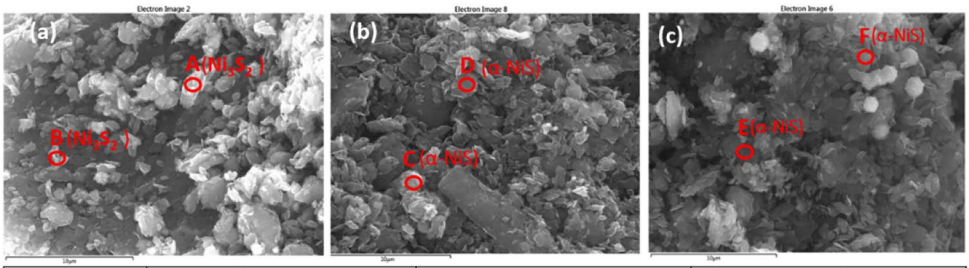

Spectrum	(a) NiS/rGO-5h		(b) NiS/rGO-10h		(c) NiS/rGO-15h	
	A at%	B at%	C at%	D at%	E at%	F at%
C	86.5	86.7	91.2	91.6	89.7	90.1
Ni	3.3	3.3	1.7	1.7	1.2	1.2
S	2.7	2.6	2.4	2.2	1.5	1.5
O	7.3	7.3	4.5	4.7	7.4	6.8
Ni:S	1.2:1	1.3:1	1:1.3	1:1.3	1:1.2	1:1.2
Estimated structure	Ni_3S_2	Ni_3S_2	α-NiS	α-NiS	α-NiS	α-NiS

Fig. 4 EDS results of NiS/rGO nanocomposite samples: **a** NiS/rGO-5 h, **b** NiS/rGO-10 h, and **c** NiS/rGO-15 h

rGO samples synthesized at 5-h, 10-h, and 15-h durations. All samples exhibited nanoflake-like spherical particles, with increasing synthesis time resulting in a rougher and more agglomerated surface morphology. The average particle sizes measured using ImageJ software were 427.9, 514.9 nm, and 463.6 nm for the 5, 10, and 15 h samples, respectively. Size distribution was determined from 80 randomly selected nanoparticles per sample.

Figure S4 presents the EDS results for the NiS/rGO nanocomposites. High carbon signals confirm the presence of rGO. The Ni:S atomic ratios derived from six marked regions (A–F) revealed phase compositions consistent with α-NiS in the 5 and 10 h samples, whereas the 15-h sample showed a ratio indicative of the Ni_3S_2 phase. Notably, after heat treatment at 450 °C for 10 min, the XRD analysis showed a transformation from α-NiS to β-NiS, indicating that thermal conditions significantly affect phase composition. This observation aligns with previous findings [26], affirming temperature-induced phase transitions in NiS structures.

Further structural insights were provided by high-resolution TEM (Fig. 5), focusing on the NiS/rGO-10 h sample. The interplanar spacing of 0.404 nm, corresponding to the (100) plane of Ni_3S_2, confirmed the crystalline nature of the nanocomposite. Autocorrelated image analysis validated the formation of single-crystal domains, consistent with the results from XRD and FESEM. These results underscore that synthesis duration and thermal treatment significantly influence the morphological and phase evolution of NiS/rGO nanocomposites, with implications for their electrochemical and catalytic performance.

The electrocatalytic activity of the NiS/rGO nanocomposites was evaluated using cyclic voltammetry (CV), showing that NiS-10 h exhibited the highest current density, outperforming Pt CEs in reducing S_x^{2-} to S^{2-}. The HR-TEM analyses (Figs. 5, S5, 6) confirmed the crystalline structure of NiS/rGO, with interplanar spacings corresponding to Ni_3S_2 and rGO planes, validating the XRD and FESEM findings. Particle size analysis (Fig. 6) revealed 17–33 nm size range, with minimal growth over time, indicating limited agglomeration. XRD confirmed phase transformation from α-NiS to β-NiS at elevated temperatures. Temperature stability tests showed that NiS/rGO retained structural and electrochemical integrity after 100 h at 25–80 °C. CV, EIS, and Tafel analyses demonstrated the superior electrocatalytic performance and thermal durability of NiS/rGO, especially for the 10-h sample, making it a promising candidate for QDSSC counter electrodes.

The structural and morphological properties of NiS/rGO nanocomposites were extensively analyzed using X-ray diffraction (XRD) and field emission scanning electron microscopy (FESEM) techniques after subjecting the samples to various reaction times (5, 10, and 15 h) and aging conditions (exposure to temperatures of 25, 40, 60, and 80 °C for 100 h). These investigations reveal the phase stability, crystallinity, and particle size evolution under different thermal conditions.

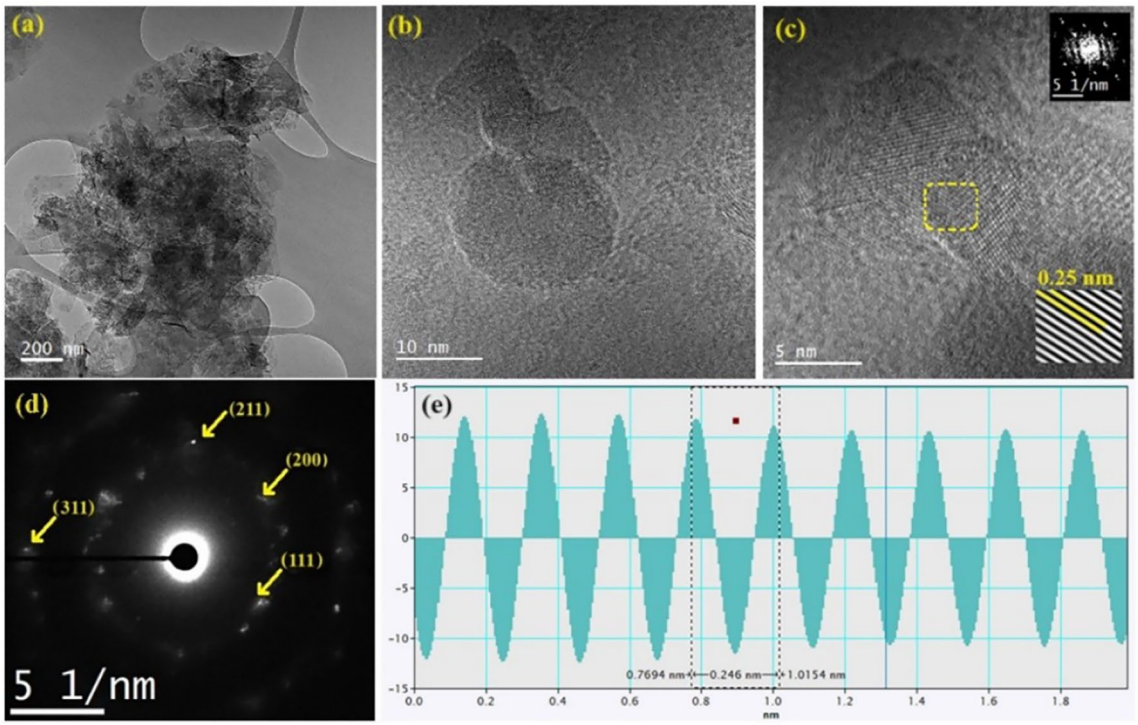

Fig. 5 HRTEM images of NiS/rGO-5 h (**a**, **b**). The inset of **c** represents the autocorrelated images of the selected portion in **b**. Bottom inset: Zoomed-in HRTEM image of the area marked with a yellow box in c. Top inset: Fast Fourier transformation (FFT) filter applied on **c**, showing the presence of a variety of crystal phases. **d** SAED pattern of Ni_3S_2 in the sample NiS/rGO-5 h, showing four diffraction circles related to unit cell planes. **e** Histogram profile of the autocorrelated images used to measure the interplanar distance corresponding to the (111) plane of Ni_3S_2

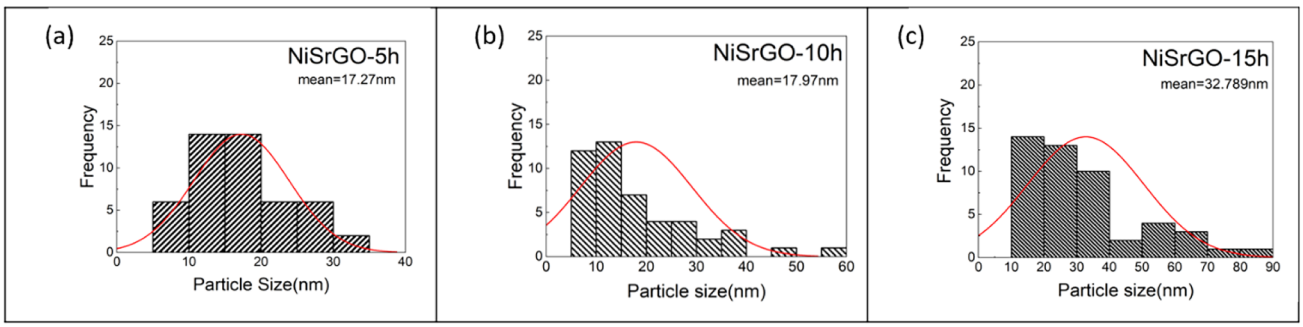

Fig. 6 Particle size distribution of the TEM results in **a** NiS/rGO-5 h, **b** NiS/rGO-10 h, and **c** NiS/rGO-15 h

3.2 Materials performance

3.2.1 Temperature stability performance

This section covers the stability performance of the NiS/rGO nanocomposites at different temperatures, assessed by two main tests. The first was an exposure test using symmetrical dummy cells of the NiS/rGO nanocomposite (5, 10, 15 h) on FTO glass substrates with polysulfide as electrolyte against exactly similar electrodes (NiS/rGO on FTO) before exposure to temperatures of 25, 40, 60, and 80 °C in an oven for 100 h. The second performance test entailed an electrocatalytic analysis, encompassing cyclic voltammetry (CV), electrochemical impedance spectroscopy (EIS), and Tafel polarization, on the NiS/rGO nanocomposites (5, 10, 15 h) in comparison to Pt CEs.

Figure S7a displays the XRD patterns of the NiS/rGO-FTO nanocomposites prepared at room temperature and aged at 25 °C for 100 h. Distinct diffraction peaks corresponding to the FTO substrate (SnO_2) are observed at 2θ values of 26.5°, 33.9°, 37.9°, 51.72°, 61.9°, 65.9°, and 78.7°, consistent with the standard rutile phase (JCPDS Card No. 00-041-1445). For the nickel sulfide phases, peaks representing β-NiS (rhombohedral, R3m space group) are detected at 18.4°, 30.3°, 32.3°, 37.5°, 51.2°, 53.8°, and 65.3° (JCPDS Card No. 01-86-2281), while α-NiS reflections appear at 30.2°, 34.7°, 46.0°, and 53.5° (JCPDS No. 00-02-1280). A broad peak near 26.5° corresponds to the (001) plane of reduced graphene oxide (rGO), confirming its incorporation. Notably, after thermal exposure, the α-NiS peaks diminished, indicating a phase transition favoring the more stable β-NiS form, aligning with the findings of [46].

Figure S7b shows that exposure at 40 °C for 100 h retains similar phase characteristics as seen at 25 °C. However, peak intensities differ, with β-NiS showing more pronounced reflections in the 5 h samples compared to the 10 and 15 h ones, suggesting superior crystallinity or particle growth in shorter reaction durations. Again, the α-NiS phase is absent post-aging, indicating thermal instability. These observations corroborate the previous studies and reinforce the preference for β-NiS formation at moderate heating.

Figure S7c presents the XRD spectra of samples exposed at 60 °C. In addition to β-NiS, new peaks are observed corresponding to Ni_3S_4, which is consistent with cubic geometry (JCPDS Card No. 00-047-7379). Prominent reflections for Ni_3S_4 are found at 32.8°, 37.7°, 64.1°, and 68.1°, indexed to the (222), (400), (533), and (444) planes, respectively. The emergence of Ni_3S_4 implies phase transformation or thermal decomposition of existing NiS into mixed nickel sulfide phases under elevated temperature exposure.

Figure S7d details the XRD data for samples aged at 80 °C. Here, β-NiS remains the dominant phase, and new peaks appear for Ni_3S_2, evident from reflections at 18.4°, 31.3°, 38.4°, 44.5°, 55.2°, 66.1°, 73.3°, and 79.0°, corresponding to the (210), (110), $(11\bar{1})$, (200), $\left(10\bar{1}\right)$, (111), $(03\bar{1})$, and (311) planes (JCPDS Card No. 00-44-1418). This transition to Ni_3S_2 at higher temperatures marks a significant structural evolution, distinct from the behavior at lower exposures.

Figures 7 and S8 illustrate the surface morphology of the NiS/rGO nanocomposites aged at 25 °C and 40 °C, respectively. At 25 °C (Fig. 7), the FESEM images reveal rough, porous surfaces with nanoflake and sponge-like morphologies, indicating efficient loading of NiS onto the rGO nanosheets. Less agglomeration is noted in the 15-h sample, suggesting improved dispersion with increased reaction time. The

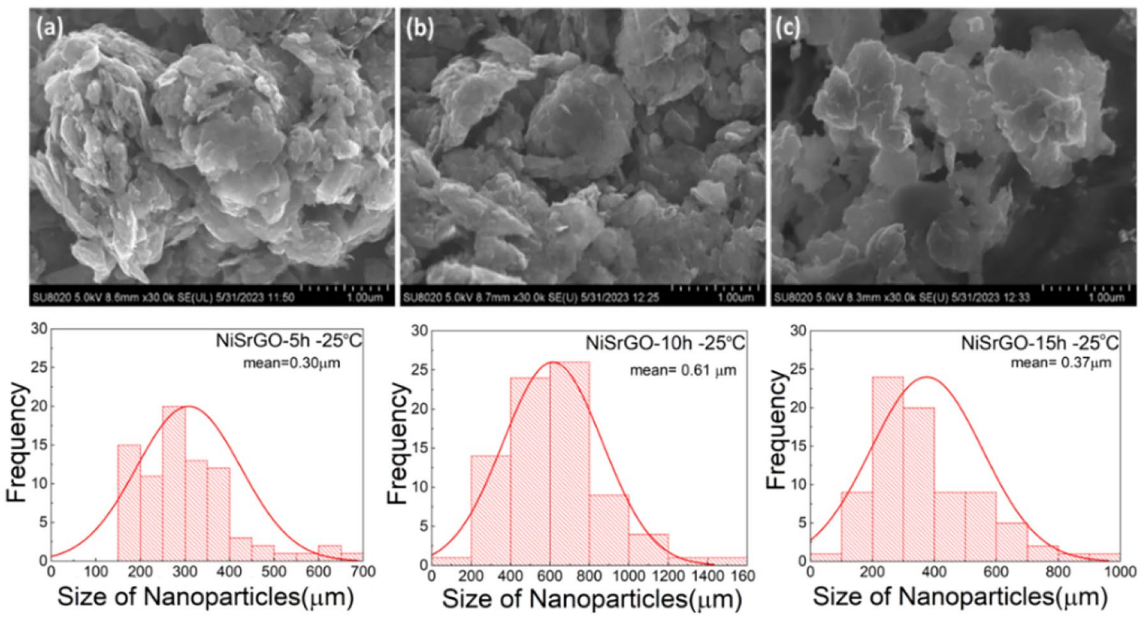

Fig. 7 FESEM images of NiS/rGO nanocomposite: **a** NiS/rGO-5 h/FTO substrate, **b** NiS/rGO-10 h/FTO substrate, **c** NiS/rGO-15 h/FTO substrate exposed to 25 °C for 100 h

size distribution analysis (based on 80 random measurements using ImageJ) yielded mean particle sizes of 306.2 nm, 613.8 nm, and 374.9 nm for 5-h, 10-h, and 15-h samples, respectively, indicating that longer synthesis time does not necessarily lead to larger particle sizes and may instead promote uniformity.

At 40 °C (Fig S8), the nanocomposites show increased porosity and interconnected sponge-like structures. Sample 5 h exhibits wider size distribution, while the 15-h sample shows smoother, rounder particles, suggesting better particle growth and uniform morphology. The average sizes recorded are 0.2 μm, 0.3 μm, and 0.4 μm for 5 h, 10 h, and 15 h, respectively. These results, supported by EDS data, show consistency in elemental composition and confirm successful deposition of NiS onto the rGO framework.

The FESEM images of the NiS/rGO nanocomposites (5, 10, and 15 h) deposited on the FTO substrates exposed to 60 °C for 100 h (Fig S9a–c) show the formation of rough, sponge-like structures with agglomeration of particles. The surface morphology of the composites varies with reaction time, with NiS/rGO 5 h exhibiting smaller agglomerates compared to the 10-h and 15-h samples. The size distribution analysis obtained from the FESEM images reveals the mean particle sizes of 0.3 μm for NiS/rGO 5 h, 0.4 μm for NiS/rGO 10 h, and 0.8 μm for NiS/rGO 15 h, as measured using ImageJ software. These values indicate that longer deposition times result in larger particle sizes, which might influence the electrochemical properties of the composites. The EDS results further confirm the increased concentration of NiS as the deposition time increased, and these findings are consistent across all samples exposed to 60 °C.

The FESEM images in Fig S10 illustrate the surface morphology of the NiS/rGO nanocomposites synthesized at different hydrothermal durations (5, 10, 15 h) and deposited on FTO glass substrates exposed to 80 °C for 100 h. NiS/rGO 5 h (Fig S10a) displays tightly packed particles without distinct rough features, indicating lower surface area. In contrast, NiS/rGO 10 h (Fig S10b) shows a porous, sponge-like morphology with more defined edges. The size distribution analysis of these samples showed average particle sizes of 0.3 μm for NiS/rGO 5 h, 0.5 μm for NiS/rGO 10 h, and 0.3 μm for NiS/rGO 15 h.

Cyclic voltammetry (CV) was used to evaluate the electrocatalytic activity of the NiS/rGO samples toward polysulfide reduction. The CV curves show a single irreversible reduction peak due to the conversion of S_x^{2-} to S^{2-}. The current density, reflecting catalytic efficiency, is highest for the NiS/rGO 5-h sample, indicating its superior electrocatalytic performance. This is consistent with literature findings. CV results at 25 and 40 °C (Fig. 8) show increased current density for NiS/rGO 5 and 15 h, while Pt and NiS/rGO 10 h had lower values. At 40 °C, Pt had the lowest current density among all, confirming that NiS/rGO materials outperformed Pt in electrocatalytic activity. NiS/rGO 5 h emerged as the most effective catalyst, with greater reduction efficiency and better stability, even with a much smaller surface area (0.2 cm^2) compared to Pt (2 cm^2). The results highlight the potential of NiS/rGO nanocomposites, particularly the 5 h sample, as promising counter electrode materials for QDSSCs.

Figure 9 illustrates the current density over 10 CV cycles for NiS/rGO nanocomposites at various temperatures (25 to 80 °C) in a polysulfide electrolyte. Among all samples, NiS/rGO-5 h exhibited the best performance, especially at higher temperatures. While its current density dropped sharply after the first cycle at 25 and 40 °C, it stabilized quickly from the second cycle onward. At 60 °C, the current density reduced gradually until the 4th cycle, then stabilized. At 80 °C, the decrease was slower and more gradual, reaching stability by the 9th cycle. In comparison, the Pt electrode showed minimal fluctuation across all temperatures, indicating better stability but lower catalytic activity.

Figure 10 confirmed that NiS/rGO 5 h consistently outperformed other composites across all tested temperatures, with current densities of 32.9 mA/cm^2 at 25 °C, 52.5 mA/cm^2 at 40 °C, 66.7 mA/cm^2 at 60 °C, and an impressive 212.5 mA/cm^2 at 80 °C. Table 1 further supports this, showing NiS/rGO-5 h maintained the highest values even after the 10th cycle at each temperature. These results confirm that NiS/rGO nanocomposites, particularly the 5-h sample, offer superior electrocatalytic performance and stability compared to Pt. Their nanoflower and nanoflake-like morphologies, with higher surface area-to-volume ratios, contribute significantly to their enhanced activity, making them highly suitable for applications involving polysulfide electrolytes, especially under elevated temperatures.

The stability of current density between the 1st and 10th cycles was compared at 25 °C for NiS Nps, NiS/rGO, Pt, and Ni_3S_4 electrodes (Fig. 11). Ni_3S_4 displayed the most stable current density over the cycles; however, NiS/rGO-5 h and NiS/rGO-15 h achieved higher current densities despite showing

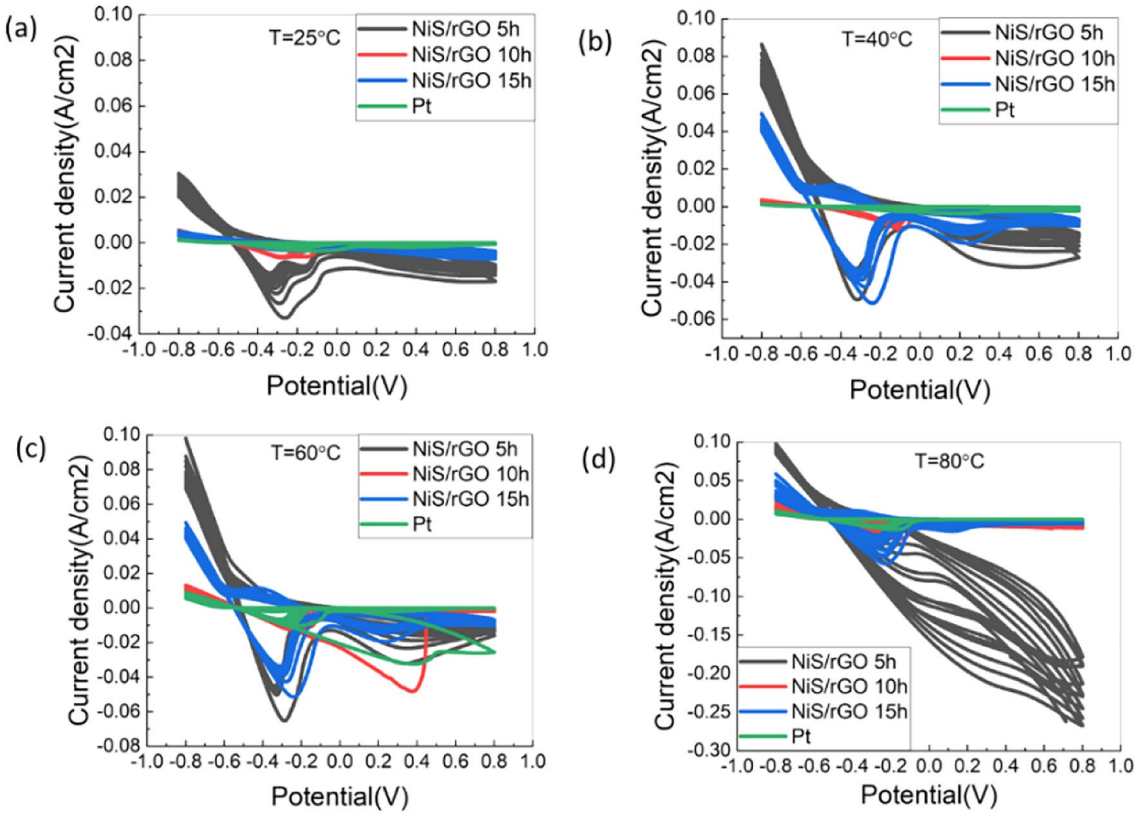

Fig. 8 Cyclic voltammograms of NiS/rGO-(5 h, 10 h and 15 h) and Pt at **a** 25 °C, **b** 40 °C, **c** 60 °C, **d** 80 °C, respectively

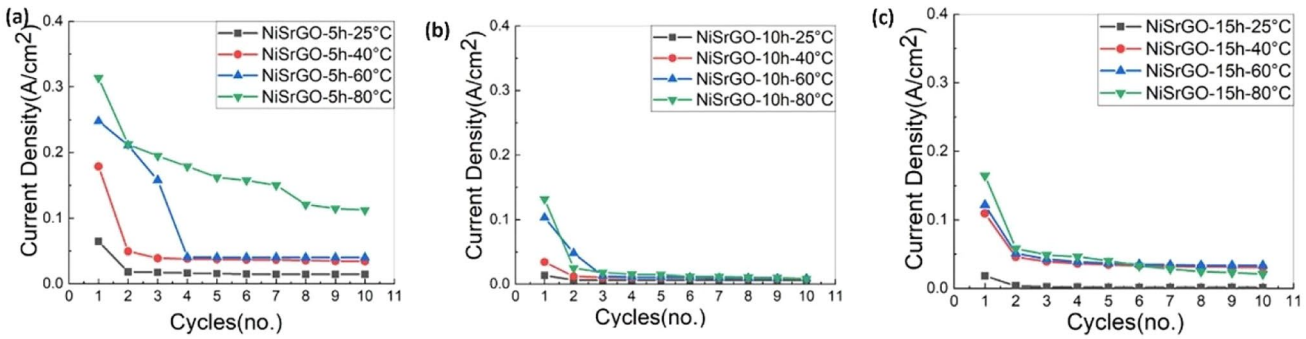

Fig. 9 Current density vs Cycles for NiS/rGO and NiS-(5 h,10 h,15 h) at various temperatures (25, 40,60, 80 °C), **a** NiS Nps-5 h, **b** NiS Nps-10 h, **c** NiS Nps-15 h, **d** NiS/rGO-5 h, **e** NiS/rGO-10 h, and **f** NiS/rGO-15 h

slightly less stability. This superior performance, particularly for NiS/rGO-5 h, is primarily attributed to the dominant presence of the β-NiS phase, which offers enhanced electrical conductivity and catalytic activity compared to the α-NiS phase. The β-NiS phase dominance was confirmed via XRD, FESEM, and HR-TEM analyses, highlighting the importance of structural and phase control in optimizing the functional performance of counter electrodes (CEs). Furthermore, comparison with previously reported data in the literature [32] demonstrates that the NiS/rGO-5 h CE exhibits competitive electrochemical stability and current density, confirming the

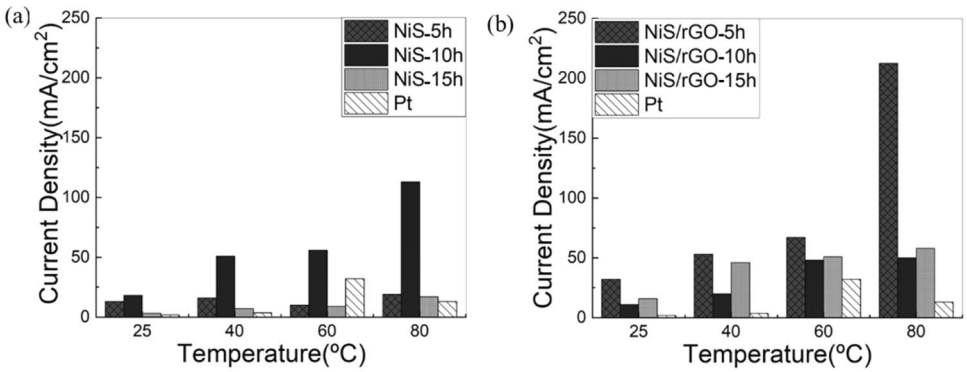

Fig. 10 Current density from 1st cycle of CV analysis at varying polysulfide testing temperatures for NiS/rGO nanocomposites synthesized at different hydrothermal reaction times (5, 10, 15 h), compared to Pt

Table 1 Current density values of samples at 1st and 10th cycles

Sample	Current density (mA/cm^2)							
	25 °C		40 °C		60 °C		80 °C	
	1st Cycle	10th Cycle	1st Cycle	10th Cycle	1st Cycle	10th Cycle	1st Cycle	10th Cycle
NiS/rGO-5 h	32.9	15.3	52.5	35.7	66.7	45.9	212.5	112.4
NiS/rGO-10 h	11.8	8.0	20.0	10.2	48.0	10.6	50.0	10.2
NiS/rGO-15 h	16.0	9.0	45.9	30.7	51.0	35.7	58.0	20.9
Pt	1.9	1.3	3.6	0.8	32.3	6.4	13.4	8.1

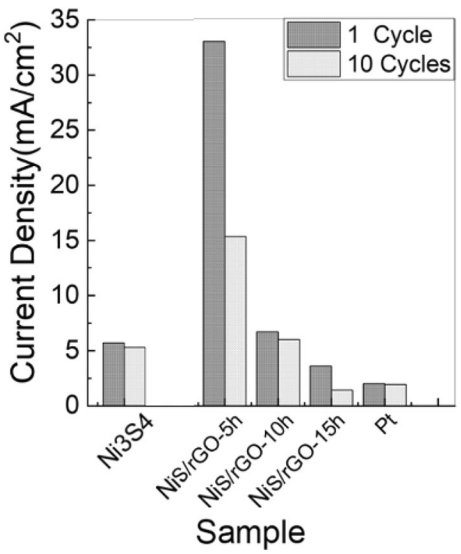

Fig. 11 Comparison of the stability in current density for one and ten cycles between the experimental results and literature * [32] at room temperature

effectiveness of the proposed synthesis strategy for improving CE.

Electrochemical Impedance Spectroscopy (EIS) was employed to evaluate the charge transfer and resistance properties of these electrodes across various temperatures (25, 40, 60, and 80 °C), using polysulfide as the electrolyte in a three-electrode system. Nyquist plots were analyzed with an equivalent circuit model comprising series resistance (R_s), charge-transfer resistance (R_{ct}), constant phase element (CPE), and Warburg impedance (Z_w) (Fig. 12).

At 25 °C, NiS/rGO-5 h exhibited the lowest R_s and R_{ct} values among all electrodes, at 1.0 Ω cm^2 and 5.0 Ω cm^2 respectively. Comparatively, NiS/rGO-10 h and NiS/rGO-15 h recorded Rs values of 2.1 Ω cm^2 and 1.7 Ω cm^2, and Rct values of 6.1 Ω cm^2 and 9.3 Ω cm^2, respectively. The Pt electrode had significantly higher resistances (R_s = 11.5 Ω cm^2, R_{ct} = 69.0 Ω cm^2), indicating poor catalytic performance. The CPE values for NiS/rGO-5, 10, and 15 h were 8.1 μF, 0.2 μF, and 0.1 μF, respectively, while the Pt CE recorded 1.3 μF. The high R_s and R_{ct} of Pt CE result in reduced fill factor and current density, highlighting its inferior efficiency compared to the NiS/rGO composites.

The low R_s in NiS/rGO-5 h signifies stronger binding between the CE material and electrode substrate, while the low R_{ct} reflects faster electron transfer at the CE/electrolyte interface. These parameters affirm NiS/rGO-5 h's superior electrochemical performance and stability. The high sulfur content in NiS/rGO-5 h

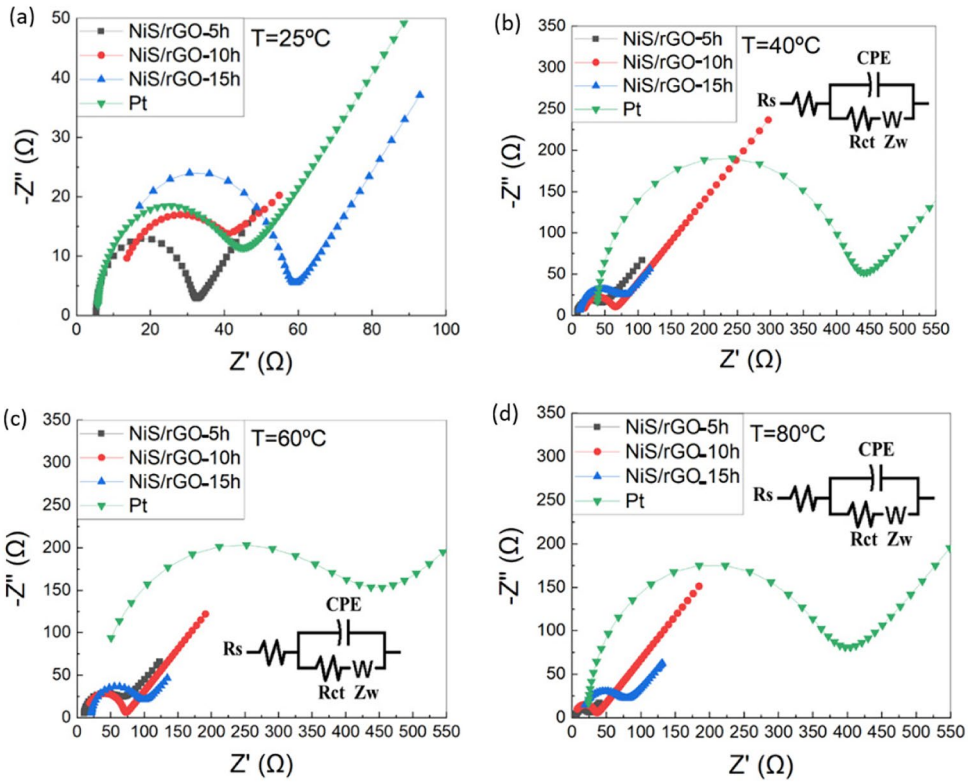

Fig. 12 Nyquist plot of NiS/rGO at different deposition times and Pt **a** at 25 °C, **b** at 40 °C, **c** at 60 °C, and **d** at 80 °C, bottom inset in equivalent circuit to simulate the EIS curves

and 10 h is also a contributing factor to their enhanced capacity for reducing S_x^{2-} to S^{2-} ions, facilitating more efficient charge transfer.

At 40 °C, the trend remained consistent. NiS/rGO-5 h maintained the lowest R_s (1.5 Ω cm^2) and R_{ct} (6.5 Ω cm^2) values, followed by NiS/rGO-10 h (R_s = 3.5 Ω cm^2, R_{ct} = 8.4 Ω cm^2), NiS/rGO-15 h (R_s = 2.4 Ω cm^2, R_{ct} = 11.3 Ω cm^2), and Pt (R_s = 75.9 Ω cm^2, R_{ct} = 749.2 Ω cm^2). These results further demonstrate the consistent advantage of NiS/rGO-5 h in terms of conductivity and catalytic activity at elevated temperatures.

At 60 °C, NiS/rGO-5 h again outperformed others, with R_s = 1.9 Ω cm^2 and R_{ct} = 6.3 Ω cm^2, compared to NiS/rGO-10 h (R_s = 2.5 Ω cm^2, R_{ct} = 11.0 Ω cm^2), NiS/rGO-15 h (R_s = 4.1 Ω cm^2, R_{ct} = 13.6 Ω cm^2), and Pt (R_s = 51.9 Ω cm^2, R_{ct} = 734.0 Ω cm^2). Despite minor variations in R_s, the significant difference in R_{ct} values confirms the superior electron transfer characteristics of NiS/rGO-5 h. The CPE values at 60 °C for NiS/rGO-5 h, 10 h, and 15 h were 0.3 μF, 0.2 μF, and 0.3 μF, respectively, further supporting enhanced electrochemical interaction at the interface.

At 80 °C, the R_{ct} of NiS/rGO-5 h was the lowest at 3.6 Ω cm^2, while its R_s stood at 1.0 Ω cm^2, nearly matching the lowest R_s recorded by NiS/rGO-10 h (0.8 Ω cm^2). NiS/rGO-15 h exhibited R_s = 2.9 Ω cm^2 and R_{ct} = 10.9 Ω cm^2, whereas the Pt CE showed R_s = 46.1 Ω cm^2 and R_{ct} = 674.4 Ω cm^2. The exceptional performance of NiS/rGO-5 h across all temperature ranges demonstrates its mechanical and electrochemical robustness, maintaining low resistance and high conductivity even at elevated temperatures.

Overall, NiS/rGO-5 h emerged as the most efficient CE, offering the best binding to the electrode surface, lowest resistance values, and highest electrocatalytic activity. Its performance is notably superior to both Pt and other NiS/rGO samples, largely due to the β-NiS phase and higher sulfur content, which enhance the reduction of polysulfide species and expedite electron transfer. The consistent low R_{ct} values across all tested temperatures reinforce the robust and effective design of NiS/rGO-5 h for applications in energy storage and conversion devices. Table 2 summarizes the electrochemical parameters of EIS for NiS/rGO nanocomposites synthesized at various reaction times (5 h, 10 h, and 15 h) and Pt in polysulfide electrolyte at 25 °C, 40 °C, 60 °C, and 80 °C.

The study presents a comparison of the EIS parameters (R_s, R_{ct}, CPE, Z_w) for the NiS/rGO nanocomposites synthesized at different times (5, 10, 15 h), along

Table 2 Electrochemical parameters of EIS for NiS/rGO nanocomposites synthesized at various reaction times (5 h, 10 h and 15 h) and Pt in polysulfide electrolyte at 25 °C, 40 °C, 60 °C, and 80 °C

Samples	Temperature(°C)	R_s	R_{ct}	CPE	Z_w ($\times 10^5$)
NiS/rGO-5 h	25	1.0	5.0	8.1	5.5
	40	1.5	6.5	0.4	13.0
	60	1.9	6.3	0.3	10.0
	80	1.0	3.6	1.1	40.0
NiS/rGO-10 h	25	2.1	6.1	0.2	12.0
	40	3.5	8.4	0.2	20.0
	60	2.5	11.0	0.2	38.0
	80	0.8	5.8	0.2	31.0
NiS/rGO-15 h	25	1.7	9.3	0.1	253.0
	40	2.4	11.3	0.2	9.0
	60	4.1	13.6	0.3	15.0
	80	2.9	10.9	0.1	6.9
Pt	25	11.5	69.0	1.3	400.0
	40	75.9	749.2	0.1	120.0
	60	51.9	734	0.1	10.0
	80	46.1	674.4	0.1	50.0

with reference materials and Pt at 25 °C (Fig S11, Table 3). NiS/rGO-5 h exhibits the lowest R_s (1 Ω cm^2) and relatively low R_{ct} (5.0 Ω cm^2), indicating superior conductivity and electrocatalytic activity compared to literature values such as NiS (R_{ct} = 11.5 Ω cm^2) and Pt (R_{ct} = 69.0 Ω cm^2). NiS/rGO-10 h and -15 h show higher R_{ct} (6.1 and 9.3 Ω cm^2, respectively). CPE values are also significantly lower for NiS/rGO-10 h (0.2 μF) and -15 h (0.1 μF) than the references, suggesting structural improvements. Zw values are the lowest for NiS/rGO-5 h (5.5×10^{-5} Ω cm^2), indicating better diffusion characteristics. The figure also compares this metal-free mechanism with traditional metal-catalyzed processes, highlighting the advantages of the former in terms of sustainability and lower environmental impact. The reaction proceeded with high efficiency, as evidenced by the consistently high yields (85–95%) obtained across different substrate types.

Tafel polarization analysis (Fig. 13, Table 4) shows that NiS/rGO-5 h has the highest corrosion current density, i_{corr} = 759.0 mA/cm^2, followed by NiS/rGO-10 h (616.5 mA/cm^2) and -15 h (255.5 mA/cm^2), suggesting the fastest reduction kinetics. Pt, in contrast, exhibits poor performance with β_a = 126.0 mV, β_c = 189.0 mV, and the lowest i_{corr}, confirming its limited catalytic efficiency in QDSSCs compared to the synthesized NiS/rGO electrodes.

For example, in one experimental setup, when the reaction was conducted at 60 °C in the presence of 1 atm of oxygen, the yield reached 92% for pyrazoline derivatives with methoxy groups at the para position on the aryl ring. The figure also shows that the metal-free oxidative hydrazonation can be performed in a variety of solvents, with DMSO providing the highest yields (up to 95%). In contrast, reactions carried out in non-polar solvents like toluene showed reduced yields of 70–75%. The comparison of yields and reaction times in different solvents emphasizes the efficiency of the method under optimized conditions.

Furthermore, the figure suggests that the metal-free oxidative hydrazonation method can be expanded to other classes of compounds, providing a sustainable route for functionalizing a variety of organic molecules. The use of oxygen as the sole oxidant makes the reaction highly environmentally friendly, and the method's ability to work without metal catalysts opens up new possibilities for large-scale, industrial applications.

These figures collectively highlight the development of a novel, sustainable method for synthesizing

Table 3 Electrochemical parameters of EIS at room temperature (25 °C) recorded for this study and literature

Sample Code	R_s (Ω cm^2)	R_{ct} (Ω cm^2)	CPE (μF)	Z_w (Ω cm^2)	References
NiS-5 h	2.9	2.0	37.6	0.6	[9]
NiS-10 h	2.2	1.4	281.9	0.1	
NiS-15 h	3.0	2.1	36.5	0.6	
NiS	4.2	11.5	36.9	14.7	[42]
Ni_3S_4	11.4	0.6	1.8	140.1	[37]
NiS/rGO-5 h	1.0	5.0	8.1	5.5×10^{-5}	This study
NiS/rGO-10 h	2.1	6.1	0.2	1.2×10^{-4}	
NiS/rGO-15 h	1.7	9.3	0.1	2.5×10^{-3}	
Pt	11.5	69.0	1.3	4×10^{-3}	

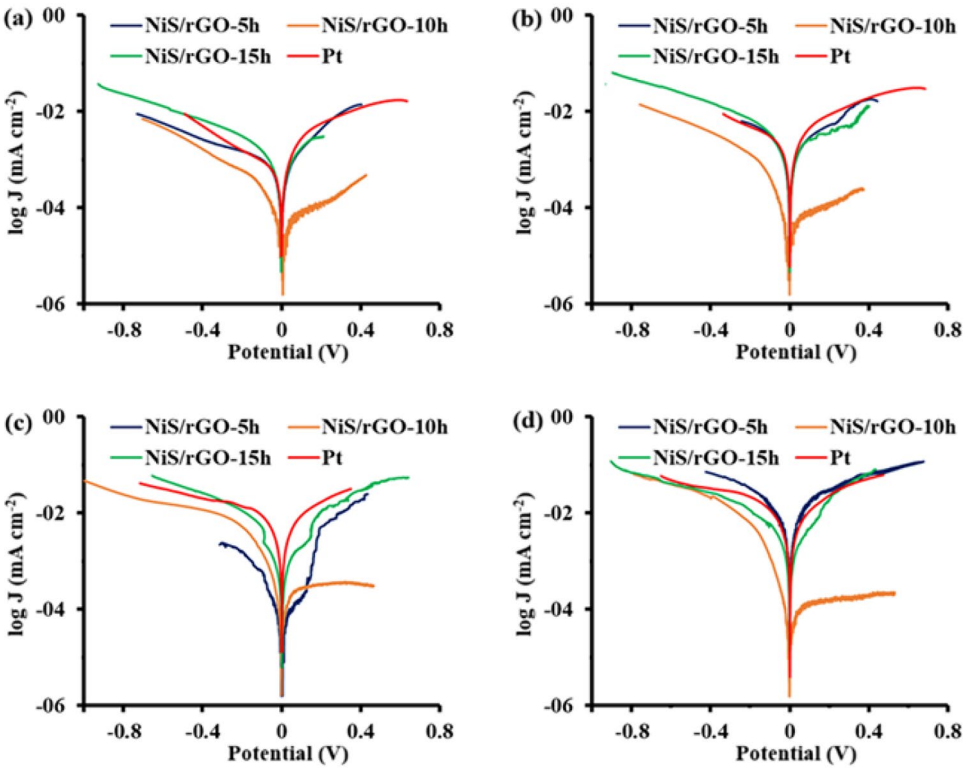

Fig. 13 Tafel polarization curves of NiS/rGO nanocomposites (5, 10, 15 h) and Pt at **a** 25 °C, **b** 40 °C, **c** 60 °C, and **d** 80 °C

Table 4 Electrochemical parameters of Tafel polarization curves for NiS/rGO nanocomposites with various hydrothermal reaction times (5, 10, and 15 h) and Pt CE at 25, 40, 60, and 80 °C

Samples	Temperature (°C)	E_{corr} (mV)	i_{corr} (mA/cm^2)	β_a (mV)	β_c (mV)
NiS/rGO-5 h	25	515.1	759.0	255.0	616.0
	40	515.6	2.2	419.1	368.6
	60	518.4	0.3	240.0	253.6
	80	521.5	13.8	370.3	517.6
NiS/rGO-10 h	25	578.4	55.0	459.0	154.0
	40	572.0	0.1	518.7	104.7
	60	667.4	0.4	236.0	152.0
	80	576.3	0.1	857.0	101.4
NiS/rGO-15 h	25	611.6	741.0	273.0	307.0
	40	651.6	1.5	476.4	274.9
	60	626.3	0.8	206.9	183.4
	80	531.7	4.3	340.2	472.7
Pt	25	578.5	0.3	126.0	189.0
	40	568.6	0.6	153.8	251.0
	60	566.4	1.1	163.3	147.6
	80	568.7	1.3	143.5	163.9

pyrazoline derivatives with high efficiency and selectivity. The metal-free oxidative hydrazonation process offers an environmentally friendly alternative to traditional metal-catalyzed reactions, with high yields and versatile applications in drug discovery and material science. The detailed analysis of reaction conditions and the impact of various substituents further underscore the potential of this method for creating tailored compounds with desirable properties.

To evaluate the catalytic properties of the prepared counter electrodes (CEs), Tafel polarization curves were measured for NiS/rGO nanocomposites with varying hydrothermal reaction times (5, 10, and 15 h) and compared to a platinum (Pt) electrode under different temperatures: 25, 40, 60, and 80 °C. Tafel polarization is an effective electrochemical method for assessing the electrocatalytic activity of materials by examining the relationship between current density and applied voltage. The Tafel curve consists of three distinct regions: the polarization zone at lower potentials, the diffusion region at higher potentials, and the Tafel zone where the slope is steep and represents the kinetics of the electrocatalytic process.

Figure 13a shows the Tafel curves for NiS/rGO-5 h, NiS/rGO-10 h, NiS/rGO-15 h, and Pt CE recorded at 25 °C. The Tafel analysis at this temperature reveals

key electrochemical parameters such as the corrosion current density (i_{corr}), corrosion potential (E_{corr}), and Tafel constants (β_a and β_c). The I_{corr} values are crucial for understanding the efficiency of electron transfer at the electrode–electrolyte interface. It was found that the I_{corr} for NiS/rGO-5 h was the highest among all the CEs, with a value of 759 mA/cm^2, indicating the fastest electron transfer process and high electrocatalytic activity. In comparison, the Pt electrode showed the lowest I_{corr} value of 255.5 mA/cm^2, reflecting poor electrocatalytic performance. The β_c value of NiS/rGO-5 h was 616.5 mV, significantly higher than the Pt value of 189.0 mV, suggesting that the reduction reaction (cathodic process) was faster than the oxidation reaction (anodic process) for NiS/rGO-5 h. In contrast, Pt exhibited a smaller βc and βa, implying poor charge transport and electrocatalytic activity at the interface of the quantum dot/electrolyte in QDSSCs. The β_a and β_c values for NiS/rGO-5 h were 255.5 mV and 616.5 mV, respectively, further demonstrating the faster reduction reaction.

Figure 13b shows the Tafel curves recorded at 40 °C for NiS/rGO-5 h, NiS/rGO-10 h, NiS/rGO-15 h, and Pt CE. At this temperature, the I_{corr} values for NiS/rGO-5 h, NiS/rGO-10 h, and NiS/rGO-15 h were 2.2 mA/cm^2, 1.5 mA/cm^2, and very low values respectively, while the Pt CE exhibited the lowest Icorr value at 0.5 mA/cm^2 indicating poor electrocatalytic activity. The β_c values for NiS/rGO-5 h, NiS/rGO-10 h, and NiS/rGO-15 h were 368.6 mV, 274.9 mV, and 307.0 mV, respectively, with NiS/rGO-5 h exhibiting the highest value, suggesting a faster reduction reaction compared to other electrodes. The β_c and β_a magnitudes for NiS/rGO-5 h were 368.6 mV and 419.1 mV, respectively, demonstrating that the reduction reaction was faster than the oxidation reaction. In contrast, Pt showed 251.0 mV for β_c and 153.8 mV for β_a, further indicating a slower electron transfer process and poor electrocatalytic activity in QDSSCs.

Figure 13c illustrates the Tafel curves recorded at 60 °C. At this higher temperature, the i_{corr} values for NiS/rGO-5 h, NiS/rGO-10 h, and NiS/rGO-15 h were 0.3 mA/cm^2, 0.4 mA/cm^2, and 0.8 mA/cm^2, respectively, while Pt still exhibited the highest Icorr value of 2.3 mA/cm^2. The β_c values for NiS/rGO-5 h, NiS/rGO-10 h, and NiS/rGO-15 h were 253.6 mV, 152.0 mV, and 183.4 mV, respectively, indicating that the reduction reaction was faster for NiS/rGO-5 h compared to the others. The β_c and β_a values for NiS/rGO-5 h were 253.6 mV and 240.0 mV, respectively, further confirming that the reduction reaction was faster than the oxidation reaction. Compared to NiS/rGO, Pt showed 147.6 mV for β_c and 163.3 mV for β_a, indicating poor electrocatalytic activity at the QD/electrolyte interface.

Figure 13d presents the Tafel curves recorded at 80 °C, where the I_{corr} values were significantly higher. NiS/rGO-5 h exhibited an i_{corr} value of 13 mA/cm^2, NiS/rGO-10 h had 0.1 mA/cm^2, and NiS/rGO-15 h showed 4.3 mA/cm^2, while Pt had an i_{corr} value of the smallest among all at 0.1 mA/cm^2, indicating poor electrocatalytic activity at this high temperature. The β_c values for NiS/rGO-5 h and NiS/rGO-15 h were 517.6 mV and 472.7 mV, respectively, which were higher than the value of 101.4 mV for NiS/rGO-10 h. The β_c and β_a values for NiS/rGO-5 h were 517.6 mV and 370.0 mV, respectively, indicating that the reduction reaction was faster than the oxidation reaction. The Pt CE exhibited 163.9 mV for βc and 143.5 mV for β_a, reflecting poor electrocatalytic activity in comparison to NiS/rGO electrodes.

The observed high i_{corr} values indicate that NiS/rGO-5 h has the fastest electron transfer process and the best electrocatalytic performance across all temperatures tested (25, 40, 60, and 80 °C). NiS/rGO-5 h showed the highest i_{corr} values at 25, 40, and 80 °C, indicating the highest intrinsic electrocatalytic activity. However, at 60 °C, Pt showed a better performance than the NiS/rGO nanocomposites, with the highest i_{corr} value of 2.3 mA/cm^2. The β_c and β_a values confirm that the reduction reaction was faster than the oxidation reaction for NiS/rGO-5 h, and the values were generally higher compared to Pt. The high i_{corr} values for NiS/rGO-5 h are consistent with the results from the electrochemical impedance spectroscopy (EIS), which further supports the superior electrocatalytic performance of this nanocomposite.

Figure 14 compares the reduction and oxidation rate values for NiS/rGO (5, 10, 15 h), Pt, and data from the reference study by [4]. The reduction rates (β_c values) were found to be higher than the oxidation rates (β_a values) in most cases, confirming that the reduction reaction is faster at the surface of the electrocatalyst. Additionally, extending the hydrothermal reaction time did not result in improved catalytic performance, as the performance of the NiS/rGO nanocomposites with longer reaction times (10 and 15 h) was inferior to that of NiS/rGO-5 h.

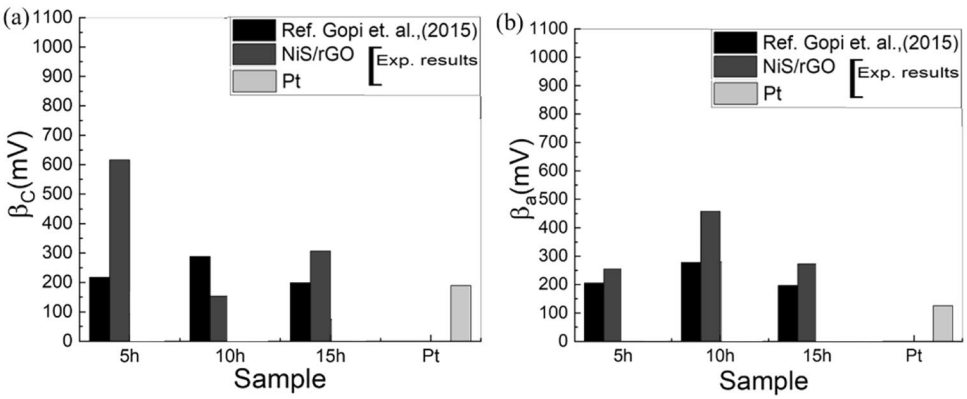

Fig. 14 Comparison of **a** reduction and **b** oxidation rate of NiS/rGO-(5, 10, 15 h), Pt and literature [4] at room temperature (25 °C)

In conclusion, the NiS/rGO-5 h composite electrode demonstrates superior electrocatalytic activity and faster electron transfer processes across a range of temperatures, with the highest i_{corr} values observed at 25, 40, and 80 °C. However, at 60 °C, Pt outperformed the NiS/rGO composites.

4 Conclusion

This research project aimed to develop nickel sulfide-based CEs to overcome catalytic sulfur poisoning, as an alternative to the well-established Pt-based counter electrodes (CEs) used in QDSSCs. Nickel sulfide and reduced graphene oxide (rGO) supported nickel sulfide-based CEs (NiS/rGO-5 h, NiS/rGO-10 h, and NiS/rGO-15 h) which were successfully synthesized by the hydrothermal method at 150 °C at varying reaction times. The synthesized CEs were well characterized using techniques like XPS, XRD, FESEM, EDS, and HR-TEM. XRD confirmed the presence of various nickel sulfide phases, including α-NiS, β-NiS, and Ni_3S_2. TEM analysis validated smaller particle sizes and showed good agreement with the XRD results via the Scherrer equation.

Electrochemical investigations, including cyclic voltammetry (CV), electrochemical impedance spectroscopy (EIS), and Tafel polarization curves, were performed to assess electrocatalytic performance. The effect of temperature on the polysulfide electrolyte (25 to 80 °C) was also investigated. rGO-supported NiS CEs outperformed Pt electrodes, with the best performance observed for NiS/rGO-5 h. This sample exhibited the highest current density during CV testing and the lowest charge-transfer resistance (R_{ct}) in EIS analysis, demonstrating excellent catalytic activity and electron transfer.

Moreover, in the investigation of Tafel polarization, the β_a, β_c, E_{corr}, and i_{corr} values of the CEs confirmed the superior behavior of the NiS/rGO-5 h nanocomposite, which showed the best electrochemical parameters among the tested samples. These findings highlight the improved electrocatalytic behavior, mechanical robustness, and thermal stability of the NiS/rGO nanocomposites.

The findings suggest that the synthesized NiS/rGO electrodes are favorable alternatives to Pt-based materials for QDSSCs. This research contributes significantly to the field of materials science, particularly in developing efficient, stable, and cost-effective solar cells. Given their high electrocatalytic activity and thermal stability, NiS/rGO nanocomposites show strong potential for commercial and industrial applications beyond QDSSCs, such as lithium–sulfur batteries, fuel cells, and supercapacitors. Future research should aim to optimize synthesis methods for the scalability, applicability, and performance of NiS/rGO nanocomposites across a broader range of energy technologies.

Author contributions

Layla Haythoor Kharboot is responsible for conceptualization, methodology, data collection, formal analysis, writing the original draft, and preparation of this work. Dr. Nor Akmal = supervision, guidance, research design, critical review, and editing of manuscript. Dr. Abdullah Sani, Dr. Tuty, Dr. Norhuda Hidayah Nordin, and Dr. Andi Erwin Eka

Putra = supervision. Dr. Ali Ataf: proofreading and editing of manuscript.

Funding

Open access funding provided by The Ministry of Higher Education Malaysia and Universiti Teknologi Malaysia. This work was financially supported by the Universiti Teknologi Malaysia under the grant scheme of UTM Fundamental Research (Q.J130000.3824.23H15) and UTMUNHAS Matching Grant (Q.J130000.3024.04M95). We thank the Material Research Consultancy Group, Faculty of Mechanical Engineering, and Universiti Teknologi Malaysia for the research support toward this publication.

Data availability

No datasets were generated or analysed during the current study.

Declarations

Conflict of interest The authors declare no competing interests.

Supplementary Information The online version contains supplementary material available at https://doi.org/10.1007/s10854-026-16855-3.

References

1. M. Shalom, I. Hod, Z. Tachan, S. Buhbut, S. Tirosh, A. Zaban, Quantum dot based anode and cathode for high voltage tandem photo-electrochemical solar cell. Energy Environ. Sci. **4**(5), 1874–1878 (2011). https://doi.org/10.1039/c1ee01145f
2. X. Zhang, X. Huang, Y. Yang, S. Wang, Y. Gong, Y. Luo, D. Li, Q. Meng, Investigation on new $CuInS_2$/carbon composite counter electrodes for CdS/CdSe cosensitized solar cells. ACS Appl. Mater. Interfaces **5**(13), 5954–5960 (2013). https://doi.org/10.1021/am400268j
3. D.M. Li, L.Y. Cheng, Y.D. Zhang, Q.X. Zhang, X.M. Huang, Y.H. Luo, Q.B. Meng, Development of Cu_2S/carbon composite electrode for CdS/CdSe quantum dot sensitized solar cell modules. Sol. Energy Mater. Sol. Cells **120**, 454–461 (2014). https://doi.org/10.1016/j.solmat.2013.09.025
4. C.V.V.M. Gopi, J.H. Bae, M. Venkata-Haritha, S.K. Kim, Y.S. Lee, G. Sarat, H.J. Kim, One-step synthesis of solution processed time-dependent highly efficient and stable PbS counter electrodes for quantum dot-sensitized solar cells. RSC Adv. **5**(130), 107522–107532 (2015). https://doi.org/10.1039/c5ra22715a
5. C.V.V.M. Gopi, S.S. Rao, S.K. Kim, D. Punnoose, H.J. Kim, Highly effective nickel sulphide counter electrode catalyst prepared by optimal hydrothermal treatment for quantum dot-sensitized solar cells. J. Power. Sources **275**, 547–556 (2015). https://doi.org/10.1016/j.jpowsour.2014.11.038
6. A.E. Reddy, S.S. Rao, C.V.V.M. Gopi, T. Anitha, C.V. Thulasi-Varma, D. Punnoose, H.J. Kim, Morphology controllable time-dependent CoS nanoparticle thin films as efficient counter electrode for quantum dot-sensitszed solar cells. Chem. Phys. Lett. **687**, 238–243 (2017). https://doi.org/10.1016/j.cplett.2017.09.001
7. R. Shwetharani, R.G. Balakrishna, One-pot synthesis of flower-like FeS_2 as counter electrode for quantum dot sensitized solar cells. Mater. Today: Proc. **9**, 594–598 (2019). https://doi.org/10.1016/j.matpr.2018.10.380
8. A.K. Prasad, J. In-Rok, S.-H. Kang, K.-S. Ahn, Novel method for synthesis of reduced graphene oxide–Cu_2S and its application as a counter electrode in

quantum-dot-sensitized solar cells. Appl. Surf. Sci. **564**, 150393 (2021). https://doi.org/10.1016/j.apsusc.2021.150393

9. G. Hodes, J. Manassen, D. Cahen, Electrocatalytic electrodes for the polysulphide redox system. J. Electrochem. Soc. **127**(3), 544–549 (1980). https://doi.org/10.1149/1.2129709
10. J.H. Zeng, D. Chen, Y.F. Wang, B.B. Jin, Graphite powder film-supported Cu_2S counter electrodes for quantum dot-sensitized solar cells. J. Mater. Chem. C **3**(46), 12140–12148 (2015). https://doi.org/10.1039/c5tc02101d
11. B. O'Regan, M. Grätzel, A low-cost, high-efficiency solar cell based on dye-sensitized colloidal TiO_2 films. Nature **353**(6346), 737–740 (1991). https://doi.org/10.1038/353737A0
12. P. Semalti, S.N. Sharma, Dye sensitized solar cells (DSSCs) electrolytes and natural photo-sensitizers: a review. J. Nanosci. Nanotechnol. **20**(6), 3647–3658 (2019). https://doi.org/10.1166/jnn.2020.17530
13. J.H. Kim, S.J. Koo, H. Cho et al., 6.16% efficiency of solid-state fiber dye-sensitized solar cells based on LiTFSI electrolytes with novel TEMPOL derivatives. ACS Sustainable Chem. Eng. **8**(40), 15065–15071 (2020). https://doi.org/10.1021/acssuschemeng.0c05427
14. M. Indhumathy, A. Prakasam, Controllable synthesis of NiS/rGO hybrid composite: an excellent counter electrode for dye sensitized solar cell. J. Clust. Sci. **31**(1), 91–98 (2019). https://doi.org/10.1007/s10876-019-01620-w
15. A. Hessein, F. Wang, H. Masai et al., Improving the stability of CdS quantum dot sensitized solar cell using highly efficient and porous CuS counter electrode. J. Renew. Sustain. Energy **9**(2), 1–12 (2017). https://doi.org/10.1063/1.4978346
16. S. Kumar, P.K. Yadav, R. Prakash et al., Multifunctional graphene oxide implanted polyurethane ionomer gel electrolyte for quantum dots sensitized solar cell. J. Alloys Compd. **922**, 1–13 (2022). https://doi.org/10.1016/j.jallcom.2022.166121
17. G. Wang, H. Wei, J. Shi et al., Significantly enhanced energy conversion efficiency of $CuInS_2$ quantum dot sensitized solar cells by controlling surface defects. Nano Energy **35**, 17–25 (2017). https://doi.org/10.1016/j.nanoen.2017.03.008
18. M.A. Basit, M.A. Abbas, E.S. Jung et al., Improved light absorbance and quantum-dot loading by macroporous TiO_2 photoanode for PbS quantum-dot-sensitized solar cells. Mater. Chem. Phys. **196**, 170–176 (2017). https://doi.org/10.1016/j.matchemphys.2017.03.057
19. Z. Pan, H. Rao, I. Mora-Seró et al., Quantum dot-sensitized solar cells. Chem. Soc. Rev. **47**(20), 7659–7702 (2018). https://doi.org/10.1039/c8cs00431e
20. H. Goodwin, T.C. Jellicoe, N.J.L.K. Davis et al., Multiple exciton generation in quantum dot-based solar cells. Nanophotonics **7**(1), 111–126 (2018). https://doi.org/10.1515/nanoph-2017-0034
21. A. Manjceevan, J. Bandara, Systematic stacking of PbS/CdS/CdSe multi-layered quantum dots for the enhancement of solar cell efficiency by harvesting wide solar spectrum. Electrochim. Acta **271**, 567–575 (2018). https://doi.org/10.1016/j.electacta.2018.03.193
22. H.J. Kim, T.B. Yeo, S.K. Kim et al., Optimal-temperature-based highly efficient NiS counter electrode for quantum-dot-sensitized solar cells. Eur. J. Inorg. Chem. (2014). https://doi.org/10.1002/ejic.201402026
23. S.A. Pawar, D.S. Patil, H.R. Jung, J.Y. Park, S.S. Mali, C.K. Hong, J.C. Shin, P.S. Patil, J.H. Kim, Quantum dot sensitized solar cell based on TiO_2/CdS/CdSe/ZnS heterostructure. Electrochim. Acta **203**, 74–83 (2016). https://doi.org/10.1016/j.electacta.2016.04.029
24. M.H. Yeh, C.P. Lee, C.Y. Chou et al., Conducting polymer-based counter electrode for a quantum-dot-sensitized solar cell (QDSSC) with a polysulfide electrolyte. Electrochim. Acta **57**(1), 277–284 (2011). https://doi.org/10.1016/j.electacta.2011.03.097
25. V.T. Chebrolu, H.J. Kim, Recent progress in quantum dot sensitized solar cells: an inclusive review of photoanode, sensitizer, electrolyte, and the counter electrode. J. Mater. Chem. C **7**(17), 4911–4933 (2019). https://doi.org/10.1039/c8tc06476h
26. G.B. Shombe, M.D. Khan, C. Zequine, C. Zhao, R.K. Gupta, N. Revaprasadu, Direct solvent-free synthesis of bare α-NiS, β-NiS and α–β-NiS composite as excellent electrocatalysts: effect of self-capping on supercapacitance and overall water splitting activity. Sci. Rep. **10**(1), 1–14 (2020). https://doi.org/10.1038/s41598-020-59714-9
27. O. Maurya, S. Khaladkar, M.R. Horn, B. Sinha, R. Deshmukh, H. Wang, T.Y. Kim, D.P. Dubal, A. Kalekar, Emergence of Ni-based chalcogenides (S and Se) for clean energy conversion and storage. Small **17**(33), 1–29 (2021). https://doi.org/10.1002/smll.202100361
28. C.V.V.M. Gopi, M. Venkata-Haritha, S.K. Kim, H.J. Kim, Improved photovoltaic performance and stability of quantum dot sensitized solar cells using Mn–ZnSe shell structure with enhanced light absorption and recombination control. Nanoscale **7**(29), 12552–12563 (2015). https://doi.org/10.1039/c5nr03291a

29. M.I. Asghar, P.D. Lund, Improving catalyst stability in nano-structured solar and fuel cells. Catal. Today **259**(2), 259–265 (2016). https://doi.org/10.1016/j.cattod.2015.05.010
30. B. Yuan, Q. Gao, X. Zhang, L. Duan, L. Chen, Z. Mao, X. Li, W. Lü, Reduced graphene oxide (RGO)/Cu_2S composite as catalytic counter electrode for quantum dot-sensitized solar cells. Electrochim. Acta **277**, 50–58 (2018). https://doi.org/10.1016/j.electacta.2018.04.218
31. J. Ali, L. Wang, H. Waseem, R. Djellabi, N.A. Oladoja, G. Pan, FeS@rGO nanocomposites as electrocatalysts for enhanced chromium removal and clean energy generation by microbial fuel cell. Chem. Eng. J. **384**, 1–11 (2020). https://doi.org/10.1016/j.cej.2019.123335
32. P. Yao, Y. Jiang, Y. Liu, C. Wu, K.C. Chou, T. Lyu, Q. Li, Catalytic effect of Ni@rGO on the hydrogen storage properties of MgH_2. J. Magnesium Alloys **8**(2), 461–471 (2020). https://doi.org/10.1016/j.jma.2019.06.006
33. A. Hessein, A.A. El-Moneim, Developing cost effective graphene conductive coating and its application as counter electrode for CdS quantum dot sensitized solar cell. Proc. World Congr. New Technol. **1**, 1–9 (2015)
34. Y. Li, Y. Chang, Y. Zhao, J. Wang, C.W. Wang, In situ synthesis of oriented NiS nanotube arrays on FTO as high-performance counter electrode for dye-sensitized solar cells. J. Alloys Compd. **679**, 384–390 (2016). https://doi.org/10.1016/j.jallcom.2016.04.079
35. A. Sarkar, A.K. Chakraborty, S. Bera, NiS/rGO nanohybrid: an excellent counter electrode for dye sensitized solar cell. Sol. Energy Mater. Sol. Cells **182**, 314–320 (2018). https://doi.org/10.1016/j.solmat.2018.03.026
36. N. Askari, A. Baghizadeh, A. Beheshti-Marnani, M.B. Askari, A. Di Bartolomeo, NiO–Co_3O_4–rGO as a multi-component transition metal oxide nanocatalyst for ultra-level detection of nitrite in beef and tap water samples. Adv. Mater. Interfaces **9**(31), 1–12 (2022). https://doi.org/10.1002/admi.202201180
37. P. Salarizadeh, M.B. Askari, A. Di Bartolomeo, MoS_2/Ni_3S_2/reduced graphene oxide nanostructure as an electrocatalyst for alcohol fuel cells. ACS Appl. Nano Mater. **5**(3), 3361–3373 (2022). https://doi.org/10.1021/acsanm.1c03946
38. A.S. Rasal, S. Yadav, A.A. Kashale, A. Altaee, J.Y. Chang, Stability of quantum dot-sensitized solar cells: a review and prospects. Nano Energy **94**, 1–32 (2022). https://doi.org/10.1016/j.nanoen.2021.106854
39. C.V.V.M. Gopi, M. Venkata-Haritha, S. Ravi, C.V. Thulasi-Varma, S.K. Kim, H.J. Kim, Solution processed low-cost and highly electrocatalytic composite NiS/PbS nanostructures as a novel counter-electrode material for high-performance quantum dot-sensitized solar cells with improved stability. J. Mater. Chem. C **3**(48), 12514–12528 (2015). https://doi.org/10.1039/c5tc03138a
40. S. Yun, P.D. Lund, A. Hinsch, Stability assessment of alternative platinum-free counter electrodes for dye-sensitized solar cells. Energy Environ. Sci. **8**(12), 3495–3514 (2015). https://doi.org/10.1039/c5ee02446c
41. U. Mehmood, A. Al-Ahmed, F.A. Al-Sulaiman, M.I. Malik, F. Shehzad, A.U.H. Khan, Effect of temperature on the photovoltaic performance and stability of solid-state dye-sensitized solar cells: a review. Renew. Sustain. Energy Rev. **79**, 946–959 (2017). https://doi.org/10.1016/j.rser.2017.05.114
42. S. Yun, P.D. Lund, Stability assessment strategy for counter electrode catalysts of dye-sensitized solar cells, in *Counter electrodes for dye-sensitized and perovskite solar cells*. (Wiley, NY, 2018), pp.395–419. https://doi.org/10.1002/9783527813636.ch16
43. X. Xu, D. Huang, K. Cao, M. Wang, S.M. Zakeeruddin, M. Grätzel, Electrochemically reduced graphene oxide multilayer films as efficient counter electrode for dye-sensitized solar cells. Sci. Rep. **3**, 1–7 (2013). https://doi.org/10.1038/srep01489
44. A.G. Kontos, T. Stergiopoulos, V. Likodimos, D. Milliken, H. Desilvesto, G. Tulloch, P. Falaras, Long-term thermal stability of liquid dye solar cells. J. Phys. Chem. C **117**(17), 8636–8646 (2013). https://doi.org/10.1021/jp400060d
45. S. Zaman, Y.Q. Su, C.L. Dong et al., Scalable molten salt synthesis of platinum alloys planted in metal–nitrogen–graphene for efficient oxygen reduction. Angew. Chem. Int. Ed. **61**(6), 1–38 (2022). https://doi.org/10.1002/anie.202115835
46. P A. Mikhaylov, M I. Vinogradov, I S. Levin, et al, Synthesis and characterization of polyethylene terephthalate-reduced graphene oxide composites. IOP Conf. Ser.: Mater. Sci. Eng. **693**, 1–8 (2019)
47. P.T. Wilkin, D.A. Rogers, Nickel sulfide formation at low temperature: initial precipitates, solubility and transformation products. Environ. Chem. **7**(6), 514–523 (2010). https://doi.org/10.1071/EN10076
48. L.L. Feng, G. Yu, Y. Wu et al., J. Am. Chem. Soc. **137**(44), 14023–14026 (2015). https://doi.org/10.1021/jacs.5b08186